Journal of Computational Chemistry

WILEY

Journal of COMPUTATIONAL CHEMISTRY

RESEARCH ARTICLE OPEN ACCESS

Photodissociation of $Cr(CO)_4bpy$: A Non-Adiabatic Dynamics Investigation

Bartosz Ciborowski | Morgane Vacher

Nantes Université, CNRS, CEISAM UMR 6230, Nantes, France

Correspondence: Morgane Vacher (morgane.vacher@univ-nantes.fr)

Received: 27 September 2024 | **Revised:** 9 December 2024 | **Accepted:** 12 December 2024

Keywords: chromium complex | non-adiabatic dynamics | photochemistry | photodissociation

ABSTRACT

Carbonyl complexes of d^6 metals with an α-diimine ligand exhibit both emission and ligand-selective photodissociation from MLCT states. Studying this photodissociative mechanism is challenging for experimental approaches due to an ultrafast femtosecond timescale and spectral overlap of multiple photoproducts. The photochemistry of a prototypical system $Cr(CO)_4bpy$ is investigated with non-adiabatic dynamic simulations. Obtained 86 fs lifetime of the bright S_3 state and 13% quantum yield are in good agreement with experimental data. The present simulations suggest a ballistic mechanism of photodissociation, which is irrespective of the occupied electronic state. This is in contrast to the previously established mechanism of competitive intersystem crossing and dissociation. Selectivity of axial photodissociation is shown to be caused by the absence of an avoided crossing in the equatorial direction.

1 | Introduction

Metal complexes with a d^6 electron configuration exhibit rich excited state behavior through a combination of an electron-rich center, closely spaced *d*-orbitals, and a shell of stabilizing and electron-accepting ligands. One of their most intriguing properties is the ligand-selective photodissociation under UV light, for instance, of a carbonyl ligand [1]. Following this process, a vacant site is formed on the metal's coordination shell, allowing for the association of a substrate. This property has been used in photocatalysis for various C–C bond-forming and breaking catalytic cycles [2, 3].

When combined with electron-accepting α-diimine ligands, such as bipyridine (bpy) or phenanthroline (phen), these complexes exhibit strong luminescence from metal-to-ligand charge transfer (MLCT) states. This property has been studied and used extensively in Re(I) [4, 5], Ru(II) [6–9], Os(II) [9], Ir(III) [10, 11] based complexes [12, 13]. $Ru(bpy)_3^{2+}$ in particular is one of the most studied lumophores, but despite this, the electronic structure of its excited state remains a point of contention [14], highlighting the complexity of transition metal systems.

A metal core with strong spin-orbit coupling with a flexible ligand shell allows for the design of versatile and tunable systems. However, rates and quantum yields of intersystem crossings are often insufficiently described by the central heavy-atom spin-orbit coupling alone [15, 16]. The interaction between nuclear, electronic, and spin degrees of freedom can lead to an intersystem crossing markedly faster [17] or slower [18] than the atomic spin-orbit coupling would predict. Ultrafast processes can also cascade to give rise to such properties as light-induced spin-crossover [19–22]. The electronic excitation may also be localized on one of the aromatic ligands and mediated by interligand charge transfer processes [23–25], which are of major importance when the complex is bound to a superstructure, such as in light-harvesting devices [26, 27]. Theoretical studies of these systems are hence necessary but challenging.

Group 6 complexes of the structure $M(CO)_4$(α-diimine) [M = Cr, Mo, W], exhibit both luminescence and photodissociation pathways from MLCT states and have been studied less so for applications but rather as model systems for spectroscopic and theoretical approaches [28–38]. The simplest of these, $Cr(CO)_4bpy$ (shown in Figure 1b), has received the most attention

and is the focus of this study as well [39–45]. While photodissociation is possible from complexes of above-mentioned metal cations, the combination of increased spin-orbit coupling for heavier metals [37] and choice of ligand can forbid or change the nature of the photodissociation pathway. In general, it occurs most prominently in complexes with both an α-diimine ligand and a carbonyl in an axial position to the α-diimine ligand. Through molecular design, dissociation of alkyl ligands [46] and from equatorial positions [47, 48] have also been achieved.

$M(CO)_4$(α-diimine) systems exhibit dual emission [49, 50] and wavelength-dependent quantum yield of photodissociation of an axial carbonyl [28–30, 39] in two energy regimes: *low* Cr→α-diimine, and *high* Cr → CO MLCT states. The *high*-energy regime is present in $M(CO)_6$ complexes, and its photodissociation is the process extensively used in photocatalysis, while the *low*-energy regime is introduced by the α-diimine ligand, and as such, its properties are sensitive to the choice of ligand and bonding to the metal. Photodissociation reactivity in the *low*-energy regime is attributed to an avoided crossing of the low $3d \rightarrow \pi^*_{bpy}$ ^{1}MLCT state with a higher lying $3d \rightarrow 3d_{x^2}$ state, shaping the lower state to a quasi-bound or dissociative shape [37, 43, 51, 52]. The strong wavelength dependence of dissociation quantum yield is understood to come from the transition to higher vibrational states, which facilitate passing over the energy barrier formed by the avoided crossing [37].

Two trapping triplet states with the lifetimes of 8 and 87 ps were identified for $Cr(CO)_4$bpy through time-resolved experiments to be the main photoproducts when excited in the *low*-energy regime [40, 42, 44]. They are understood to be the source of emission and in direct competition with the photodissociation pathway. With picosecond triplet lifetimes, their depopulation is the limiting step for the femtosecond dissociation process. Conversely, if luminescence is of interest, then photodissociation is an undesirable substrate-depleting process.

Previous experimental works by Farrell, Matousek, and Vlček [42, 44] have reported that photodissociation completes within 400 fs. Later work by Ma et al. [45] has shown, through better temporal resolution, that this process finishes within 100 fs. Exact photodissociation rate could not be obtained due to spectral overlap of absorption with triplet states and a low quantum yield, so an estimate of $(\sim 2.3\ \text{ps})^{-1}$ was given, based on an assumption of competitive branching between photodissociation and intersystem crossing to ^{3}MLCT states. The quantum yield of photodissociation for the *low*-energy $3d \rightarrow \pi^*_{bpy}$ states ranges from 1% to 10%, depending on experimental conditions [29, 39].

To the best of our knowledge, the only previous theoretical work to use dynamic methods on $Cr(CO)_4$bpy is that of Guillaumont, Vlček, and Daniel [41, 43]. They calculated MRCI/CASSCF potential energy surfaces (PES), which we use as reference data, and propagated a nuclear wavepacket in one dimension. We aim to expand on insights of that study by using non-adiabatic simulations in full dimensionality, using the surface hopping method [53, 54].

Our objectives are to obtain nuclear dynamic information and use it to refine the mechanism of this ultrafast photodissociation process by determining the origins of ligand selectivity and establishing the extent of competition between photodissociation and intersystem crossing.

In Section 2, we present the theoretical methods used in the present study. In Section 3, we begin by reporting the results of benchmarking electronic structure methods along the Cr–CO_{ax} stretching coordinate, followed by the results of surface hopping dynamic simulations. We then discuss the obtained results in the context of previous literature.

2 | Methods

All calculations in this work were performed in the gas phase. The equilibrium geometry of the electronic ground state was optimized at B3LYP/6-31G* level of theory (structure shown in Table S3) in OpenMolcas [55], under C_{2v} symmetry constraint. It has been shown previously to give good Cr–C and C–O

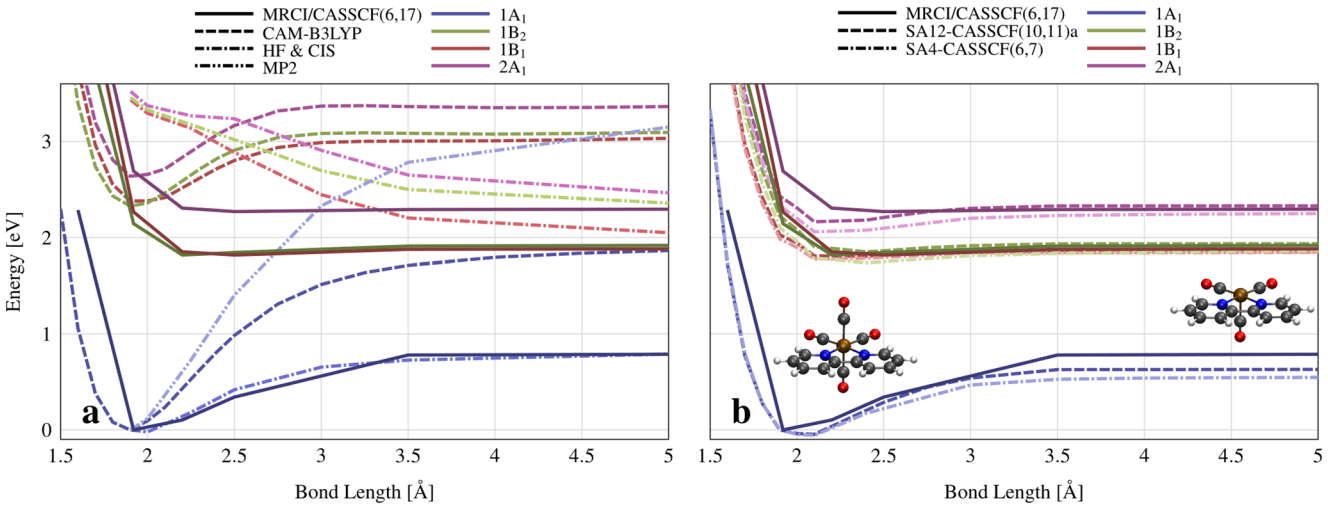

FIGURE 1 | Singlet potential energy curves as a function of Cr–CO_{ax} bond length; (**a**) Single reference methods; (**b**) SA-CASSCF methods; Reference MRCI/CASSCF(6,17) data reproduced from Guillaumont, Vlček, and Daniel [43]; The scans were initiated from a B3LYP/6-31G* minimum geometry; orbitals included in each active space are detailed in text. State labels correspond to the symmetry at C_{2v} Franck-Condon (FC) geometry.

bond lengths in $Cr(CO)_6$ [56]. TD-DFT excitation energies with B3LYP, PBE0, BHHLYP, and CAM-B3LYP functionals and 6-31G*, 6-311G*, 6-31+G*, and 6-311+G* basis sets were calculated at the B3LYP/6-31G* minimum geometry in ORCA 5.0.3 [57] (Tables S1 and S2) to evaluate the accuracy of TD-DFT and its sensitivity to chosen functional and basis.

Next, rigid potential energy scans along the Cr–CO_{ax} bond stretching coordinate were calculated using HF/CIS, MP2, and TD-DFT, compared against MRCI/CASSCF reference data [43] (Figure 1a). The reference data features a CASSCF(6,17) ground state and MRCI/CASSCF(6,17) excited states: A CASSCF(6,17) solution with a CISD calculation on each reference with a contribution of > 0.08 to the CASSCF state. Due to the poor performance of single-reference methods, calculations were performed with State Averaged CASSCF in OpenMolcas (Figures 1b and S3). Several active spaces were attempted, but due to active space- and symmetry-breaking issues, only five CASSCF scans were completed successfully. The tested active spaces were composed of: (1) AS(6,7) three pairs of metal bonding/antibonding orbitals ($3d_{xz}$, $3d_{z^2-y^2}$, $3d_{xy}$), plus the first π^* orbital of bipyridine; (2) AS(10,11)a—additional two pairs of π / π^* bipyridine orbitals; (3) AS(10,11)b—adding remaining metal orbital pairs to AS(6,7) ($3d_{x^2}$, $3d_{yz}$) (see Figure S1). CASSCF solutions were calculated state-averaging over 4 states for AS(1) and 12 states for AS(2); AS(3) was calculated state-averaging over 4, 7, and 12 states, giving five methods: SA4-CASSCF(6,7), SA12-CASSCF(10,11)a, SA4-CASSCF(10,11)b, SA7-CASSCF(10,11)b, and SA12-CASSCF(10,11)b. All CASSCF calculations were performed with the ANO-RCC-VDZ basis set.

SA4-CASSCF(6,7) was selected for use in surface hopping [53, 54] calculations. Four singlet and three triplet states were used as active states, and so triplet SA3-CASSCF(6,7) PES were additionally calculated, along with SA4-CASSCF(6,7) CO_{eq} PES (shown in Figures S3d and S4, respectively). Dynamics calculations were performed using SHARC 3.0 software, [58, 59] interfaced with OpenMolcas. A 0K Wigner distribution of 100 geometries and velocities was randomly generated at the SA4-CASSCF(6,7) minimum geometry (structure shown in Table S5) using SHARC. All sampled geometries were initiated on the S_3 state, which is the bright $3d_{xz} \rightarrow \pi^*_{bpy}$ state. Trajectories were propagated with local diabatization [60], energy-based decoherence [61, 62] (empirical parameter of 0.1 au), in the diagonal representation, using a timestep of 0.5 fs. Two electronic structure calculations were performed at each timestep, SA4-CASSCF(6,7) for singlet states and SA3-CASSCF(6,7) for triplet states, giving state energies and gradients for all 7 considered states, both using the ANO-RCC-VDZ basis set. Spin-orbit coupling effects were included through the Douglas-Kroll Hamiltonian to second order.

Two criteria of energy conservation were used to stop trajectories: (1) a deviation of 0.3 eV of total energy from the beginning of trajectory; (2) a step of 0.25 eV total energy during a single timestep. Additionally, individual state energies of all trajectories were monitored for breakdown of the active space. Trajectories for which the active space was unstable were stopped, regardless of their total energy. These trajectories contribute to all data analyses up until the failure point, after which the data is renormalized, if required. The majority of stopped trajectories were caused by the instability of the active space: in total, 20 out of 100 at 300 fs and 37 out of 100 at 400 fs. All remaining trajectories were calculated up to 400 fs, which is taken as the simulation end point for the ensemble, but several trajectories were continued beyond to 600 fs in order to investigate nuclear evolutions on longer timescales.

3 | Results and Discussion

First presented are PES along the Cr–CO_{ax} bond stretching coordinate for studied methods (initial benchmark of excited state methods at the Franck-Condon (FC) region is presented in SI). Then, results of surface hopping dynamic simulations are shown and discussed, split into nuclear and electronic dynamics. Finally, insights from combined electronic and nuclear dynamics are presented.

3.1 | Potential Energy Scans

Potential energy curves of single-reference methods are compared against high-level MRCI/CASSCF(6,17) data in Figure 1a. All studied states are of $3d \rightarrow \pi^*_{bpy}$ MLCT character. The highest singlet S_3, denoted $2A_1$ as per its FC symmetry, is a $3d_{xz} \rightarrow \pi^*_{bpy}$ state. The lower S_2 and S_1 states, denoted $1B_1$ and $1B_2$, are of $3d_{z^2-x^2} \rightarrow \pi^*_{bpy}$ and $3d_{xy} \rightarrow \pi^*_{bpy}$ characters, respectively. See Figure S1 in ESI for orbital graphical representations. The high-level MRCI/CASSCF(6,17) [43] curves feature a ground state barrier of ~0.8 eV, and excited states show shallow minima. All single reference methods fail to qualitatively capture the ground state shape of PES. HF follows the reference ground state very closely, not showing any failure. UHF and UKS calculations of several functionals all give the spin operator value $\langle S^2 \rangle$ of 0.0 along the entire reaction coordinate, showing that a ground state dissociation produces two singlet products, and is of singlet character throughout. The ground state of CAM-B3LYP has a significantly overestimated energy barrier of ~1.9 eV. The transition energies at FC and dissociation-limit geometries are in excellent agreement with MRCI/CASSCF(6,17), but intermediate geometries give overestimated energies of up to 0.5 eV (see Figure S2). Independently of this, the erroneous shape of the ground state renders all excited states non-dissociative. The same PES calculations were repeated with all DFT functionals available in ORCA 5.0.3 (not shown) to investigate if this is a functional or method-dependent problem. All have produced the same overestimated ground state energy barrier, showing that DFT is fundamentally unable to describe this bond-breaking process and that a different method needs to be used. MP2 shows typical failure of describing dissociation processes, based on which ADC(2) calculations were not attempted. These considerations have led us to consider CASSCF as the method of choice.

Potential energy curves of SA4-CASSCF(6,7) and SA12-CASSCF(10,11)a are shown in Figure 1b. All CASSCF variants qualitatively reproduce the shape of reference curves. SA4-CASSCF(6,7) and SA12-CASSCF(10,11) a show minimum ground state geometries with bond lengths of 2.1 Å (1.9 Å for MRCI/CASSCF(6,17) and B3LYP) and excited state energy barriers: ~0.1 eV for S_1 and S_2; ~ 0. 2 eV for S_3 (0.1 eV and 0.02 eV for MRCI/CASSCF(6,17)). Interestingly, neither method explicitly includes orbitals or states involved in avoided crossings between $3d \rightarrow 3d_{x^2}$ and lower excited states, which are well established in

literature to be the cause of quasi-bound excited state shapes [37]. Reference MRCI/CASSCF(6,17) data does not include the relevant $3d_{x^2}$ orbital in its active space either, but this interaction is expected to be incorporated through the post-CASSCF CISD calculation (although not for the ground state, which is just CASSCF(6,17)). Analysis of the CASSCF solution shows that, as the bond stretches, the π^*_{bpy} orbital gains a contribution from the $3d_{x^2}$ basis function (see Table S4). CASSCF(10,11)b calculations (Figure S3a), which explicitly include the relevant d_{x^2} orbital at FC geometry, show a much greater contribution of $3d_{x^2}$ basis function as the bond stretches, clearly showing state mixing. Points at which the contribution of this basis function increases considerably coincide with the local maxima and onsets of plateaus in CASSCF(10,11)b.

For SA4-CASSCF(10,11)b, the ground state curve has a maximum at 3.0 Å and strongly underestimated energies beyond that point. S_1 and S_2 state curves remain nearly unchanged, while S_3 now features a gentle maximum at the same coordinate as the ground state. In SA7-CASSCF(10,11)b, the ground state no longer has a local maximum, but all three excited states do. Simultaneously, they have significantly higher excitation energies throughout the entire curve, but more so near the FC region. The states S_4, S_5, and S_6 (not shown) are all of $3d \rightarrow 3d_{x^2}$ character at extended bond lengths (they are strongly mixed at the FC region) and all feature a local minimum at the same geometry as the maxima of lower states. This method clearly captures the avoided crossing but is, as a whole, of much worse quality. These characteristics are augmented further in SA12-CASSCF(10,11)b, where all excited states are dissociative and have higher excitation energies. Our attempts at explicitly incorporating the avoided crossing have brought behavior that is more different from MRCI/CASSCF(6,17) and at a greater computational cost. The smaller active space, SA4-CASSCF(6,7), produces the most quantitatively agreeable behavior, and so it was chosen to be used in further dynamic calculations.

To complete static studies, PES for triplet states were calculated at the SA3-CASSCF(6,7) level of theory (see Figure S3d). Calculated triplets are the analogues to the excited states of SA4-CASSCF(6,7). T_1 and T_2 are almost coincident in energy outside of the FC region. The character of triplet states, assigned based on contributing orbital transitions, is discontinuous around 2.00–2.75 Å. This suggests the existence of an accessible conical intersection seam between 1^3A_1 and 1^3B_1, or T_3 and T_2 states. This would enable quick depopulation of the T_3 state and support the observation of only two emissive triplet states [42]. The energy barrier of both T_1 and T_2 is under 0.1 eV, which is lower than for singlet states.

PES singlet curves of Cr–CO_{eq} were calculated using SA4-CASSCF(6,7) (see Figure S4). Ground state in this coordinate has a higher energy barrier of 1.2 eV and excited state barriers of 0.7–1.0 eV. Furthermore, the π^*_{bpy} orbital gains no contribution from the $3d_{x^2}$ orbital upon elongation of the bond, due to its perpendicular position to the CO_{eq} ligand. This directionality of the avoided crossing is consistent with ligand selectivity of photodissociation. Simultaneously, the excited energy barriers are low enough to allow for equatorial dissociation if a complex is designed with an appropriate metal center and ligands, which both stabilize axial bonds and destabilize equatorial bonds.

From a simple electrostatic picture, Cr→bpy excitations lead to the depopulation of the metal center. This leaves less electron density for bonding between Cr and CO. Consequently, *any* Cr→bpy excitation would have a photodissociative effect, regardless of spin, which is in line with CO being a spectator ligand of the excitation process. Indeed, the lowering of excited state energy barriers is observed along both CO_{ax} and CO_{eq} dissociations, but the absence of $3d_{x^2}$ avoided crossing results in bound shapes of the excited states along CO_{eq} dissociation pathway.

3.2 | Electronic Dynamics

The evolution of Molecular Coulomb Hamiltonian (MCH) active state electronic populations is presented in Figure 2. The bright S_3 state starts decaying instantly and fits well with a monoexponential decay function with a lifetime of 86 fs (over 300 fs, $R^2 = 0.981$). This is in good agreement with the solvent-independent experimental value of 96 fs [45]. Electronic population of T_3 and T_2 never exceeds 0.05 and 0.1, respectively. T_1 rises approximately linearly during 50–300 fs, reaching a plateau of ∼0.19. Calculating triplet state lifetimes would require much longer simulation times, but the existence of a T_1 plateau does indicate a much slower decay to S_0, in accordance with their measured picosecond lifetimes [42, 45]. The ground state population increases in a semi-stepwise manner, with three flat regions at 0 fs, ∼120 fs, and ∼300 fs. The first two regions suggest that transitions to the ground state are favored at stretched bond geometries (discussed below), while the third is more likely due to the exhaustion of higher singlet state population and dephasing of coherent oscillations.

To complement electronic population data, the total count of hopping events and the net difference of downwards and upwards hops are presented in Table 1. The resulting approximate mechanism is shown in Figure 3. The main transfer of population goes through a cascade of $S_3 \rightarrow S_2 \rightarrow S_1 \rightarrow S_0$, with branching points $S_2 \rightarrow T_3$ and $S_1 \rightarrow T_2$, and non-negligible direct transfer of $S_3 \rightarrow S_1$. $S_3 \rightarrow S_2$ transitions appear to occur mainly at the very beginning of the simulation, suggesting that this is the only allowed transition in the FC region. The 'middle' states S_2, S_1, T_3, and T_2 are in dynamic equilibrium, owing to low energy separation, but with a net flow towards S_1 and T_2. From there, trajectories decay either via $S_1 \rightarrow S_0$ or $T_2 \rightarrow T_1$. Transitions to S_0 are mostly irreversible, though some back hops are observed. The S_0 state energy is frequently close to the 'middle' manifold during a trajectory, but once a transition to S_0 occurs, ground and excited state energies quickly diverge, preventing back hops. This is true even if a dissociating trajectory drops to the ground state, suggesting that this is due to a nuclear rearrangement of the complex, fully coordinated or not. Finally, there is a dynamic equilibrium between T_2 and T_1, which is in agreement with the observed two trapping triplet states [37, 42]. The lack of direct transfer $S_{1-3} \rightarrow T_1$ is in accordance with previous observations [45]. The apparent equilibrium between T_1 and S_0, as judged by the number of hops in Table 1, is due to low energy gaps and state mixing on trajectories in the T_1 state. The low net transfer into T_3 and T_2 states does not allow for a confident confirmation of the existence of a T_3/T_2 conical intersection, which was suggested by calculated PES.

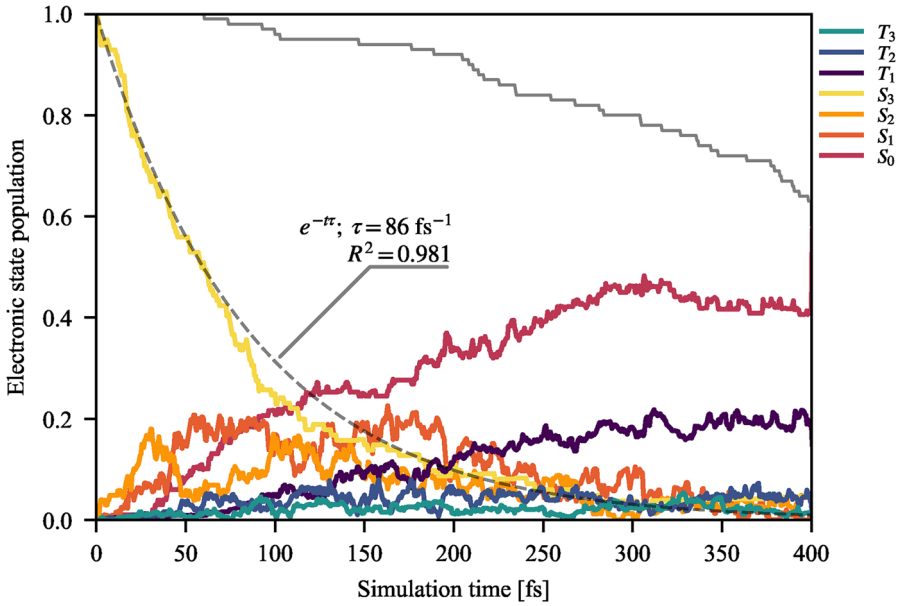

FIGURE 2 | Time evolution of the electronic active state MCH populations. Trajectories that ended early stopped contributing at the time of failure, and the ensemble is renormalized over the remaining trajectories. Gray solid line indicates the fraction of remaining trajectories. Gray dashed line is the monoexponential fit of S_3 decay over 300 fs.

TABLE 1 | Number of MCH hopping events within 300 fs. Transitions are from states in the first column to states in the first row. Top: Total count; Bottom: Net difference between downward and upward hops.

↗	S_0	S_1	S_2	S_3	T_1	T_2	T_3
S_0	—	16	1	4	64	6	0
S_1	57	—	85	3	8	235	50
S_2	8	121	—	11	0	2	62
S_3	12	34	62	—	0	1	5
T_1	64	3	0	0	—	42	5
T_2	6	215	3	0	61	—	17
T_3	0	56	54	0	4	22	—
↗	S_0	S_1	S_2	S_3	T_1	T_2	T_3
S_0	—						
S_1	41	—			5	20	
S_2	7	36	—				8
S_3	8	31	51	—		1	5
T_1					—		1
T_2			1		19	—	
T_3		6				5	—

3.3 | Nuclear Dynamics

For each trajectory, the evolution of the two equivalent Cr–CO_{ax} bonds was tracked, and the one that has reached a greater value is shown in Figure 4a. The bond length of all Cr–CO_{eq} is shown in Figure S5. No dissociation of an equatorial ligand was observed,

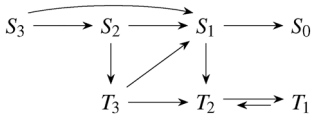

FIGURE 3 | Proposed mechanism for the main deactivation pathway of $Cr(CO)_4bpy$.

in accordance with literature [42]. For all trajectories, if the Cr–CO_{ax} bond length has passed 3.5 Å, it was not observed to drop back below this value, so it was chosen as the threshold after which a trajectory is considered dissociated. Upon excitation to the S_3 state, all trajectories begin stretching their Cr–CO bonds. For CO_{ax} (CO_{eq}), they begin at ~2.02 (1.92) Å and oscillate between 2.0 (1.9) and 2.3 (2.1) Å with a period of ~150 (80) fs. Upon reaching the first maximum of Cr–CO_{ax}, most trajectories proceed back down the oscillation pathway, while a small subset evolves towards longer bond lengths. Of this subset, some do not dissociate, instead taking a longer arc down, or hovering close to 3.0 Å for over 100 fs. The remaining other trajectories proceed beyond this avoided crossing region and dissociate.

At 400 fs, 9 out of 70 trajectories were observed to dissociate (7 dissociated trajectories were stopped before 400 fs), and all did so as a continuation of the upward motion of the Cr–CO_{ax} oscillation, giving a quantum yield of 13%. It is in rough agreement with experimental work, where it ranges from 1% to 10%, depending on experimental conditions [29, 39]. Seven trajectories dissociated during the first period, and two more in the second period. One additional trajectory dissociated beyond 400 fs, on the third period.

To investigate the importance of other motions, Figure 4b presents the time evolution of selected frequency-mass scaled normal coordinates ν. For each mode i, the mean displacement μ_i and standard deviation σ_i (also referred to as *activity*)

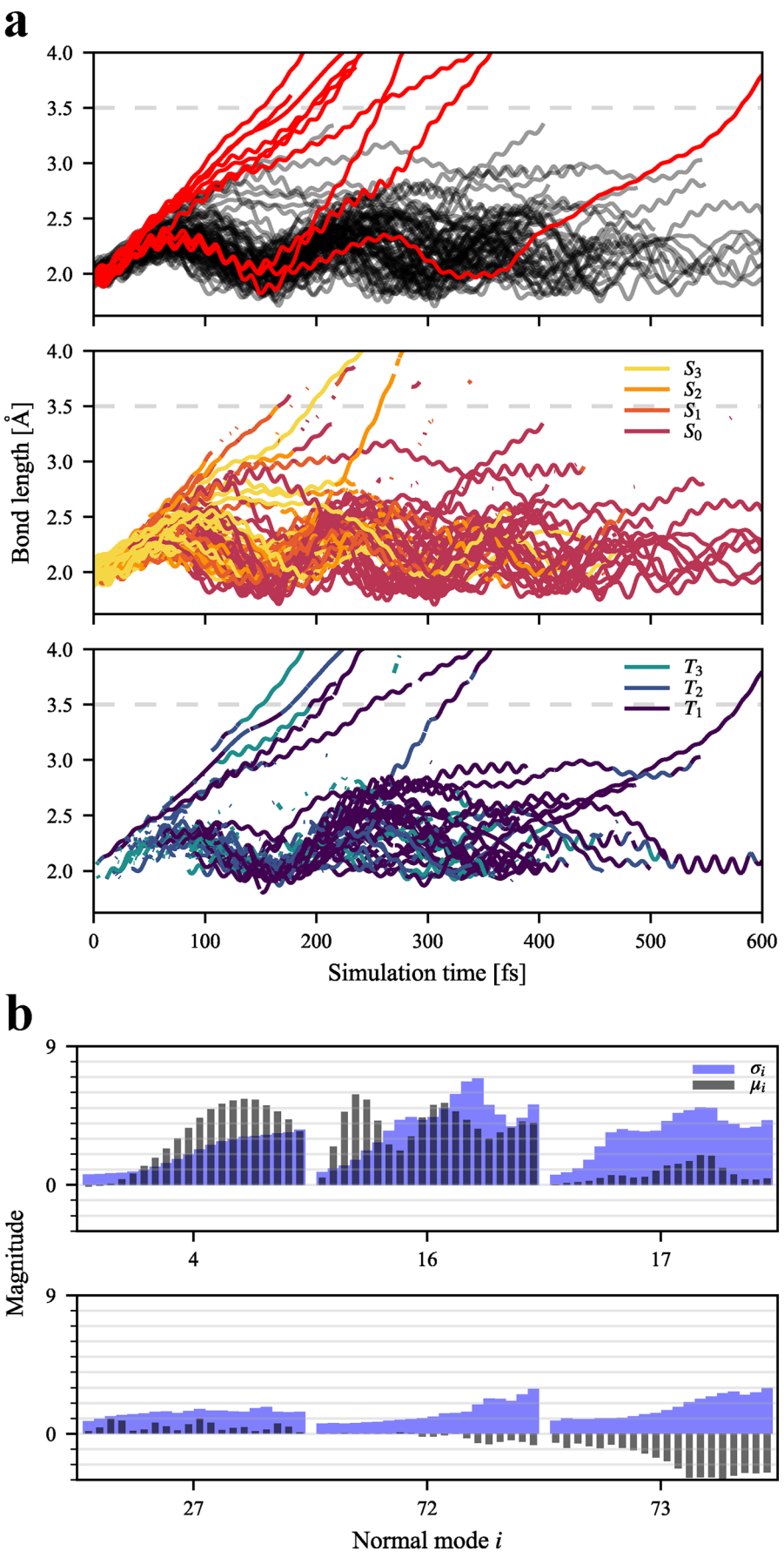

FIGURE 4 | Legend on next page.

are presented in grey and blue, respectively. These parameters were averaged in time slices of 20 fs, up to 400 fs. Analysis of all modes is shown in Figure S6. The majority of normal modes show minimal temporal change. Those which vary most in time all involve carbonyl ligands: ν_{72} and ν_{73} are the antisymmetric and symmetric axial C-O stretching modes, ν_{16} and ν_{17} are symmetric and antisymmetric Cr–CO_{ax} stretching modes, and ν_4 involves $_{ax}$OC-Cr–CO_{ax} bending in the *xz*-plane, with a lesser contribution of equatorial $_{eq}$OC-Cr–CO_{eq} bending.

Several modes are set in motion in a coherent manner upon the initial electronic excitation: ν_{12} and ν_{14}, which both have strong contributions from symmetric stretching of Cr-N bonds; ν_{22}, the symmetric stretch of Cr-CO_{eq}; ν_{19}, ν_{35}, ν_{38}, ν_{45}, ν_{60}, ν_{64}, and ν_{66}, which are all stretching modes of bipyridine bonds; ν_{27}, which involves OC-Cr-CO and Cr-C-O bending of all carbonyl ligands. Of these, only modes ν_{22} and ν_{27} show a sizeable change in activity over time.

Several low-frequency modes, in particular axial C-Cr-C bending ν_4, increase in activity in a semi-stepwise manner and not immediately upon excitation. The onset of this sharp increase happens at around 100 fs, which is the same period of time at which the Cr–CO_{ax} bond length was noted to diverge between dissociation, contraction, or hovering for an extended period. When considering dissociating trajectories alone (Insets of Figure S6), the activity of ν_{16} and ν_{17} is much greater, while the activity of ν_4 is considerably reduced, though the mean displacement remains high in both. This behavior suggests a coupling between Cr–CO_{ax} stretching and $_{ax}$OC-Cr–CO_{ax} bending modes, which would act to inhibit dissociation.

These observations suggest a ballistic model of the photodissociation process. Looking again at PES of Figure 1, the S_3 state has a downward gradient away from the FC region at 2.02 Å, which is the center of the initial Wigner distribution. This slope gives the system kinetic energy towards dissociation. For most trajectories, this is not enough to overcome the energy barrier: The bond contracts back. A smaller subset will have kinetic energy that is approximately equal to the barrier. These trajectories will hover in the avoided crossing region plateau, on top of the energy barrier, before turning back after an extended period. Finally, those with even more energy will overcome the barrier with sufficient leftover kinetic energy to continue the motion towards dissociation on a flat surface. This is supported by the observation that the initial bond lengths of all dissociating trajectories are in the shorter half of the initial Wigner distribution. As time proceeds, for non-dissociating trajectories, the excess energy within this oscillating normal mode is expected to equipartition into other modes of motion, making the dissociation less likely after subsequent periods. In other words, if a trajectory did not dissociate during the first period of bond oscillation (around 150 fs), it is less likely to dissociate later on. It is still possible as a probabilistic process, and three trajectories in total were observed to dissociate on second and third periods, but in significantly lesser numbers. It is also noted that solvent may prohibit dissociation after the first period of oscillation. A ballistic model is consistent with the ∼100 fs timescale of photodissociation [42, 45] and wavelength-dependence of the quantum yield, as occupying a higher vibrational state will directly favor dissociation. The evolution of Cr–CO_{eq} (Figure S5) shows no dissociation. When compared with Cr–CO_{ax}, shorter periods of oscillation (80 vs. 150 fs) and shorter bond lengths at minimum geometry (1.92 vs. 2.02 Å) indicate a stronger bond, consistent with the bound shape of PES and higher energy barriers (Figure S4). Slight overestimation of the photodissociation quantum yield is a possible consequence of neglecting solvent effects. An explicit solvent could act as a physical barrier for the released molecule, shifting the energy barrier upwards, as well as damping vibrational motion, prohibiting dissociation beyond the first period of Cr–CO_{ax} oscillation.

3.4 | Combined Nuclear and Electronic Dynamics

In this section, we combine the electronic and nuclear dynamic information, seen on the middle and bottom panels of Figure 4a. Seven out of ten dissociating trajectories are of triplet character at 3.5 Å. Five of these trajectories undergo intersystem crossing long before reaching the energy barrier at ∼3.0 Å; the remaining two do so in its vicinity. This is in contrast to the established understanding that triplet states are non-dissociative. It is, however consistent with the calculated PES, wherein T_1 and T_2 have lower energy barriers of dissociation than all singlet states. Therefore, if a trajectory undergoes intersystem crossing early on, it will approach a lower energy barrier and be more likely to cross it. This supports the above-explained mechanism, where the main determining factor is the energy barrier and not the occupied electronic and spin state.

A remaining question is how the nuclear conformation affects the probability of transitions. Cannizzo et al. [63] have noted a correlation between metal-ligand vibrational frequencies and intersystem crossing time scales for analogous systems $Re(L)(CO)_3(bpy)$ [L = Cl, Br, I]. This suggests that a distortion along the ligand-metal stretching mode leads to an area with greater spin-orbit coupling and favoured intersystem crossings. Similar observations were noted for the lifetimes of singlet MLCT states in Fe and Ru tris-bpy complexes [8, 64]. In present simulations, the semi-stepwise increase of S_0 population points towards a similar behavior.

To investigate the coupling between nuclear motions and electronic spin transitions, Figure 5a presents: (1) energy gap between states S_1 and T_2; (2) norm of the spin-orbit coupling matrix element (SOCME), averaged over all trajectories as a function of normal mode displacement, for selected modes. A full plot over all modes is presented in Figure S7. We focus on the S_1/T_2 crossing, as it accounts for over half of all ISC hops (Table 1).

FIGURE 4 | (**a**) Evolution of Cr–CO_{ax} bond length of all trajectories. Top: colored red if a trajectory reached 3.5 Å (threshold indicated by an horizontal dashed line). Middle and Bottom: coloured by currently occupied MCH state, split into singlet (middle) and triplet (bottom) states. (**b**) Mean displacement μ_i and standard deviation σ_i for selected mass-frequency scaled normal modes i of the trajectory ensemble. Average values were taken over each 20 fs interval, up to the final value of 400 fs.

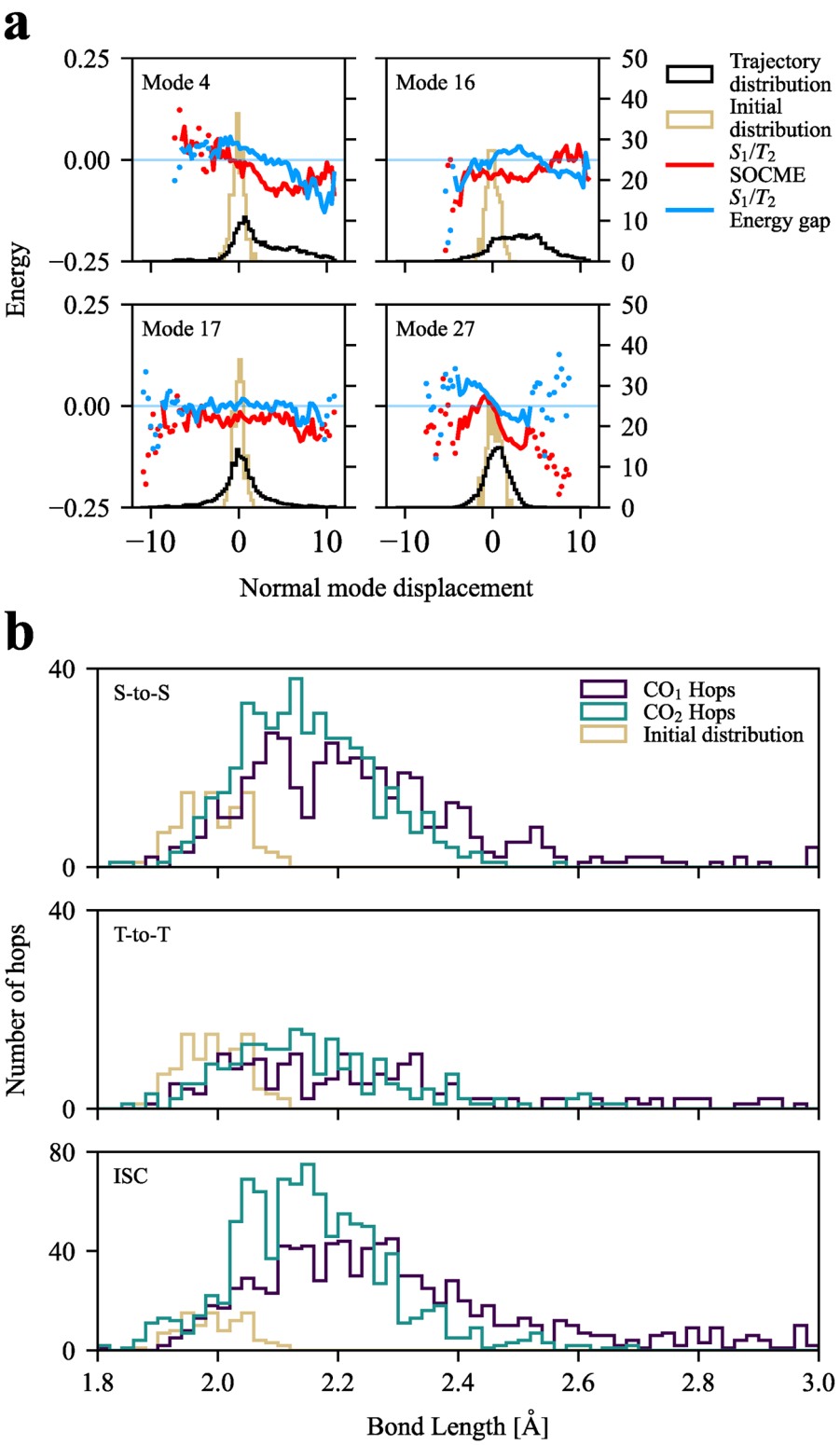

FIGURE 5 | (**a**) Energy gap and spin-orbit coupling matrix elements of S_1/T_2 crossing, averaged over the nuclear displacement of selected normal modes. The distribution of all geometries visited during dynamics and the initial Wigner distribution are given for reference. Energy gap values are given in eV (left axis) and SOCME are given in cm^{-1} (right axis). Areas with under 100 samples are indicated with dots; (**b**) Histograms of all observed hops as a function of Cr–CO_{ax} bond length. For each trajectory, the farther-reaching CO_{ax} is denoted CO_1, and the other CO_2. Initial distribution is shown in red.

Variation of SOCME was not observed to be large enough to indicate a favorable ISC at particular geometries. All states in the middle manifold (S_{1-2} and T_{1-3}) were observed to evolve in parallel; that is, the pairwise energy gap remained near constant. For the S_1/T_2 pair, the energy gap was very close to degeneracy, as can be seen most clearly for mode ν_{17}. A weak dependence of energy gap on nuclear displacement was noted for various bending modes involving Cr-L bonds, with example modes ν_4 and ν_{27}

being shown. The symmetric Cr–CO_{ax} stretching mode does also show a weak dependence, and with the previously shown coupling with ν_4, they would account for a weakly favoured ISC at extended Cr–CO_{ax} geometries. However, the near-degeneracy of these two states remains as the dominant driving force for ISC. Figure 5b shows distributions of all hops and the initial Wigner distribution as a function of Cr–CO_{ax} bond length. For each trajectory, hops are shown against bond lengths of both CO_{ax}, with the one that has reached the farthest denoted CO_1; the other CO_2. CO_2 acts as a control distribution, approximating one that would statistically arise from vibrational motion alone. For CO_1 (CO_2), the median of initial distribution is 1.99 Å while the distributions of hops have medians of 2.21, 2.24, and 2.27 Å (2.14, 2.12, and 2.14 Å) for $S \rightarrow S$, $T \rightarrow T$, and intersystem crossing hops, respectively. Comparison of CO_1 and CO_2 distributions shows that ISC hops are weakly favored at stretched bond geometries, in accordance with the above analysis of energy gap dependence.

4 | Conclusions

We have theoretically investigated the photochemistry of $Cr(CO)_4$bpy with surface hopping non-adiabatic dynamics in combination with CASSCF for the electronic structure. The calculated photodissociation quantum yield of an axial CO ligand is 13% and the predicted lifetime of S_3 bright state is 86 fs, both in good agreement with experimental data [29, 39, 45]. The initial excited state decays to a middle manifold of S_2, S_1, T_3, and T_2 electronic states, which are in fast dynamic equilibrium, owing to small state energy differences, with a net flow towards S_1 and T_2. From there, the system decays to the ground state via the $S_1 \rightarrow S_0$ transition or is trapped in a dynamic equilibrium $T_2 \leftrightarrow T_1$. The flow of electronic population into the triplet equilibrium, weakly influenced by bending modes around the central chromium atom, is in direct accordance with the experimental presence of triplet trapping states. The present simulations show involvement of S_1 and S_2 states, which were not observed previously. The simulations show that the initial relaxation of the S_3 bright state is not a competitive process between photodissociation and intersystem crossing. Photodissociation is instead a ballistic process that can occur from both singlet and triplet states. It happens within 150 fs as the kinetic energy along the reactive mode of motion quickly dissipates into other modes. Equatorial carbonyls are not observed to dissociate, having higher energy dissociation barriers due to a lack of an avoided crossing with higher-lying $3d_{x^2}$ states.

Acknowledgments

This work is funded by the European Union (ERC 101040356-ATTOP) and *Région des Pays de la Loire*. Views and opinions expressed are however, those of the authors only and do not necessarily reflect those of the European Union or the European Research Council Executive Agency. Neither the European Union nor the granting authority can be held responsible for them. This work received financial support from the State through the EUR LUMOMAT project and the Investissements d'Avenir program ANR-18-EURE-0012. Calculations were performed at Centre de Calcul Intensif des Pays de la Loire, GLiCID, located in Nantes. The authors are thankful to Denis Jacquemin for fruitful discussions and to the Institute for Development and Resources in Intensive Scientific Computing (IDRIS) for allocation of computational time.

Data Availability Statement

The data that support the findings of this study are available from the corresponding author upon reasonable request.

References

1. S. A. Trushin, W. Fuss, W. E. Schmid, and K. L. Kompa, "Femtosecond Dynamics and Vibrational Coherence in Gas-Phase Ultraviolet Photodecomposition of $Cr(CO)_6$," *Journal of Physical Chemistry A* 102, no. 23 (1998): 4129–4137.

2. T. Szymańska-Buzar, "Photochemical Reactions of Group 6 Metal Carbonyls Catalytic Transformation of Alkenes and Alkynes," *Coordination Chemistry Reviews* 159 (1997): 205–220.

3. T. Szymańska-Buzar, "Photochemical Reactions of Group 6 Metal Carbonyls With Alkenes," *Coordination Chemistry Reviews* 250, no. 9 (2006): 976–990.

4. D. R. Striplin and G. A. Crosby, "Photophysical Investigations of Rhenium(I)Cl$(CO)_3$(Phenanthroline) Complexes," *Coordination Chemistry Reviews* 211, no. 1 (2001): 163–175.

5. K. K.-W. Lo, M.-W. Louie, and K. Y. Zhang, "Design of Luminescent Iridium(III) and Rhenium(I) Polypyridine Complexes as In Vitro and In Vivo Ion, Molecular and Biological Probes," *Coordination Chemistry Reviews* 254, no. 21 (2010): 2603–2622.

6. A. Juris, V. Balzani, F. Barigelletti, S. Campagna, P. Belser, and A. von Zelewsky, "Ru(II) Polypyridine Complexes: Photophysics, Photochemistry, Eletrochemistry, and Chemiluminescence," *Coordination Chemistry Reviews* 84 (1988): 85–277.

7. S. A. McFarland, F. S. Lee, K. A. W. Y. Cheng, F. L. Cozens, and N. P. Schepp, "Picosecond Dynamics of Nonthermalized Excited States in Tris(2,2-Bipyridine)ruthenium(II) Derivatives Elucidated by High Energy Excitation," *Journal of the American Chemical Society* 127, no. 19 (2005): 7065–7070.

8. A. Cannizzo, F. van Mourik, W. Gawelda, G. Zgrablic, C. Bressler, and M. Chergui, "Broadband Femtosecond Fluorescence Spectroscopy of $[Ru(bpy)_3]^{2+}$," *Angewandte Chemie, International Edition* 45, no. 19 (2006): 3174–3176.

9. P.-T. Chou and Y. Chi, "Osmium- and Ruthenium-Based Phosphorescent Materials: Design, Photophysics, and Utilization in OLED Fabrication," *European Journal of Inorganic Chemistry* 2006, no. 17 (2006): 3319–3332.

10. M. K. Nazeeruddin, R. Humphry-Baker, D. Berner, S. Rivier, L. Zuppiroli, and M. Graetzel, "Highly Phosphorescence Iridium Complexes and Their Application in Organic Light-Emitting Devices," *Journal of the American Chemical Society* 125, no. 29 (2003): 8790–8797.

11. P.-Y. Ho, C.-L. Ho, and W.-Y. Wong, "Recent Advances of Iridium(III) Metallophosphors for Health-Related Applications," *Coordination Chemistry Reviews* 413 (2020): 213267.

12. R. C. Evans, P. Douglas, and C. J. Winscom, "Coordination Complexes Exhibiting Room-Temperature Phosphorescence: Evaluation of Their Suitability as Triplet Emitters in Organic Light Emitting Diodes," *Coordination Chemistry Reviews* 250, no. 15 (2006): 2093–2126.

13. V. Fernández-Moreira, F. L. Thorp-Greenwood, and M. P. Coogan, "Application of d^6 Transition Metal Complexes in Fluorescence Cell Imaging," *Chemical Communications* 46 (2010): 186–202.

14. P. Dongare, B. D. B. Myron, L. Wang, D. W. Thompson, and T. J. Meyer, "$[Ru(bpy)_3]^{2+*}$ Is It Localized or Delocalized? How Does It Decay?," *Coordination Chemistry Reviews* 345 (2017): 86–107.

15. M. Chergui, "On the Interplay Between Charge, Spin and Structural Dynamics in Transition Metal Complexes," *Dalton Transactions* 41 (2012): 13022–13029.

16. T. J. Penfold, E. Gindensperger, C. Daniel, and C. M. Marian, "Spin-Vibronic Mechanism for Intersystem Crossing," *Chemical Reviews* 118, no. 15 (2018): 6975–7025.

17. O. Bräm, F. Messina, A. M. El-Zohry, A. Cannizzo, and M. Chergui, "Polychromatic Femtosecond Fluorescence Studies of Metal-Polypyridine Complexes in Solution," *Chemical Physics* 393, no. 1 (2012): 51–57.

18. R. M. van der Veen, A. Cannizzo, F. van Mourik, A. Vlček Jr, and M. Chergui, "Vibrational Relaxation and Intersystem Crossing of Binuclear Metal Complexes in Solution," *Journal of the American Chemical Society* 133, no. 2 (2011): 305–315.

19. S. Decurtins, P. Gütlich, C. P. Köhler, H. Spiering, and A. Hauser, "Light-Induced Excited Spin State Trapping in a Transition-Metal Complex: The Hexa-1-Propyltetrazole-iron (II) Tetrafluoroborate Spin-Crossover System," *Chemical Physics Letters* 105, no. 1 (1984): 1–4.

20. A. Cannizzo, C. J. Milne, C. Consani, et al., "Light-Induced Spin Crossover in Fe(II)-based Complexes: The Full Photocycle Unraveled by Ultrafast Optical and X-Ray Spectroscopies," *Coordination Chemistry Reviews* 254, no. 21 (2010): 2677–2686.

21. M. Pápai, G. Vankó, T. Rozgonyi, and T. J. Penfold, "High-Efficiency Iron Photosensitizer Explained With Quantum Wavepacket Dynamics," *Journal of Physical Chemistry Letters* 7, no. 11 (2016): 2009–2014.

22. M. Pápai, "Toward Simulation of Fe(II) low-Spin ? High-Spin Photoswitching by Synergistic Spin-Vibronic Dynamics," *Journal of Chemical Theory and Computation* 18, no. 3 (2022): 1329–1339.

23. A. T. Yeh, C. V. Shank, and J. K. McCusker, "Ultrafast Electron Localization Dynamics Following Photo-Induced Charge Transfer," *Science* 289, no. 5481 (2000): 935–938.

24. B. Pettersson Rimgard, J. Föhlinger, J. Petersson, et al., "Ultrafast Interligand electron Transfer in cis-[Ru(4,4′-Dicarboxylate-2,2′-Bipyridine)$_2$(NCS)$_2$]$^{4-}$ and Implications for electron Injection Limitations in Dye Sensitized Solar Cells," *Chemical Science* 9 (2018): 7958–7967.

25. F. Perrella, X. Li, A. Petrone, and N. Rega, "Nature of the Ultrafast Interligands Electron Transfers in Dye-Sensitized Solar Cells," *JACS Au* 3, no. 1 (2023): 70–79.

26. E. I. Mayo, K. Kilså, T. Tirrell, et al., "Cyclometalated iridium (III)-sensitized titanium dioxide solar cells," *Photochemical & Photobiological Sciences* 5 (2006): 871–873.

27. P. G. Bomben, K. C. D. Robson, P. A. Sedach, and C. P. Berlinguette, "On the Viability of Cyclometalated Ru(II) Complexes for Light-Harvesting Applications," *Inorganic Chemistry* 48, no. 20 (2009): 9631–9643.

28. M. S. Wrighton and D. L. Morse, "The Nature of the Lowest Excited State and Photosubstitution Reactivity of Tetracarbonyl-1,10-Phenanthrolinetungsten(0) and Related Complexes," *Journal of Organometallic Chemistry* 97, no. 3 (1975): 405–419.

29. R. W. Balk, T. Snoeck, D. J. Stufkens, and A. Oskam, "(Diimine) carbonyl Complexes of Chromium, Molybdenum, and Tungsten: Relationship Between Resonance Raman Spectra and Photosubstitution Quantum Yields Upon Excitation Within the Lowest Metal to Diimine Charge-Transfer Band," *Inorganic Chemistry* 19, no. 10 (1980): 3015–3021.

30. D. M. Manuta and A. J. Lees, "Emission and Photochemistry of M(CO)4(Diimine) (M = Chromium, Molybdenum, Tungsten) Complexes in Room-Temperature Solution," *Inorganic Chemistry* 25, no. 9 (1986): 1354–1359.

31. K. Kalyanasundaram, "Time-Resolved Studies on the Dynamics of Photoinduced Formation of M(CO)$_4$(Polypyridyl) (M = Molybdenum, Chromium and Tungsten) Complexes," *Journal of Physical Chemistry* 92, no. 8 (1988): 2219–2223.

32. S. Wieland, K. B. Reddy, and R. Van Eldik, "Ligand-Field and Charge-Transfer Photochemistry of M(CO)$_4$ (1,10-Phenanthroline) (M= Chromium, Molybdenum, Tungsten) Mechanistic Information From High-Pressure Effects," *Organometallics* 9, no. 6 (1990): 1802–1806.

33. W.-F. Fu and R. van Eldik, "Photo-Substitution Reactions of Cr(CO)$_4$(1,10-Phenanthroline). Mechanistic Information From Entering Nucleophile, Irradiation Wavelength and Pressure Dependences," *Inorganica Chimica Acta* 251, no. 1 (1996): 341–346.

34. W.-F. Fu and R. van Eldik, "Photosubstitution Reactions of M(CO)$_4$(1,10-Phenanthroline) (M = Mo, W) Influence of Entering Ligand, Irradiation Wavelength, and Pressure," *Organometallics* 16, no. 4 (1997): 572–578.

35. W.-F. Fu and R. van Eldik, "Systematic Tuning of the Photosubstitution Mechanism of M(CO)$_4$ (1,10-Phenanthroline) by Variation of the Metal, Entering Nucleophile, Excitation Wavelength, and Pressure," *Inorganic Chemistry* 37, no. 5 (1998): 1044–1050.

36. I. R. Farrell, J. van Slageren, S. Záliš, and A. Vlček Jr, "Time-Resolved Emission Spectra and TD-DFT Excited-State Calculations of [W(CO)4(1,10-Phenanthroline)] and [W(CO)$_4$(3,4,7,8-Tetramethyl-1,10-Phenanthroline)]," *Inorganica Chimica Acta* 315, no. 1 (2001): 44–52.

37. A. Vlček Jr, "Highlights of the Spectroscopy, Photochemistry and Electrochemistry of [M(CO)$_4$(α-Diimine)] complexes, M=Cr, Mo, W," *Coordination Chemistry Reviews* 230, no. 1 (2002): 225–242.

38. M. Röhrs and D. Escudero, "Multiple Anti-Kasha Emissions in Transition-Metal Complexes," *Journal of Physical Chemistry Letters* 10, no. 19 (2019): 5798–5804.

39. J. Víchová, F. Hartl, and A. Vlček Jr, "Wavelength-Dependent Photosubstitution and Excited-State Dynamics of [Cr(CO)4(2,2′-Bipyridine)]: A Quantum Yield and Picosecond Absorption Study," *Journal of the American Chemical Society* 114, no. 27 (1992): 10903–10910.

40. I. G. Virrels, M. W. George, J. J. Turner, J. Peters, and A. Vlček Jr, "Photochemistry of Cr(CO)$_4$(bpy) (bpy = 2,2'-Bipyridine) Studied by Time-Resolved Infrared Spectroscopy," *Organometallics* 15, no. 19 (1996): 4089–4092.

41. D. Guillaumont, C. Daniel, and A. Vlček Jr, "Electronic Structure of the Lowest Excited States of Cr(CO)4(2,2′-Bipyridine): A CASSCF/CASPT2 Analysis," *Inorganic Chemistry* 36, no. 8 (1997): 1684–1688.

42. I. R. Farrell, P. Matousek, and A. Vlček Jr, "Femtosecond Spectroscopic Study of MLCT Excited-State Dynamics of Cr(CO)4(Bpy): Excitation-Energy-Dependent Branching Between CO Dissociation and Relaxation," *Journal of the American Chemical Society* 121, no. 22 (1999): 5296–5301.

43. D. Guillaumont, A. Vlček Jr, and C. Daniel, "Photoreactivity of Cr(CO)4(2,2'-Bipyridine): Quantum Chemistry and Photodissociation Dynamics," *Journal of Physical Chemistry. A* 105, no. 7 (2001): 1107–1114.

44. I. R. Farrell, P. Matousek, M. Towrie, et al., "Direct Observation of Competitive Ultrafast CO Dissociation and Relaxation of an MLCT Excited State: Picosecond Time-Resolved Infrared Spectroscopic Study of [Cr(CO)$_4$(2,2′-Bipyridine)]," *Inorganic Chemistry* 41, no. 17 (2002): 4318–4323.

45. F. Ma, M. Jarenmark, S. Hedström, P. Persson, E. Nordlander, and A. Yartsev, "Ultrafast Excited State Dynamics of [Cr(CO)4(Bpy)]: Revealing the Relaxation Between Triplet Charge-Transfer States," *RSC Advances* 6 (2016): 20507–20515.

46. A. Gabrielsson, A. M. Blanco-Rodríguez, P. Matousek, M. Towrie, and A. Vlček Jr, "Different Mechanisms of Photochemical Re-Me and Re-Et Bond Homolysis in [Re(R) (CO)$_3$(4,4′-Dimethyl-2,2′-Bipyridine)] A Time-Resolved IR Spectroscopic Study Ranging From Picoseconds to Microseconds," *Organometallics* 25, no. 9 (2006): 2148–2156.

47. A. Gabrielsson, S. Záliš, P. Matousek, M. Towrie, and A. Vlček Jr, "Ultrafast Photochemical Dissociation of an Equatorial CO Ligand From Trans(X,X)-[Ru(X)$_2$(CO)$_2$(bpy)] (X = Cl, Br, I): A Picosecond Time-Resolved Infrared Spectroscopic and DFT Computational Study," *Inorganic Chemistry* 43, no. 23 (2004): 7380–7388.

48. A. Gabrielsson, M. Towrie, S. Záliš, and A. Vlček Jr, "Nanosecond CO Photodissociation and Excited-State Character of [Ru(X)(X')(CO)$_2$(N,N'-diisopropyl-1,4-diazabutadiene)] (X = X' = Cl or I; X = Me, X' = I; X =

$SnPh_3$, X′ = Cl) Studied by Time-Resolved Infrared Spectroscopy and DFT Calculations," *Inorganic Chemistry* 47, no. 10 (2008): 4236–4242.

49. P. C. Servaas, H. K. Van Dijk, T. L. Snoeck, D. J. Stufkens, and A. Oskam, "Relationship Between the Emission Spectra and Resonance Raman Excitation Profiles of $W(CO)_4$(α-diimine) Complexes," *Inorganic Chemistry* 24, no. 26 (1985): 4494–4498.

50. D. J. Stufkens, "Spectroscopy, Photophysics and Photochemistry of Zerovalent Transition Metal α-Diimine Complexes," *Coordination Chemistry Reviews* 104, no. 1 (1990): 39–112.

51. A. Rosa, G. Ricciardi, E. J. Baerends, and D. J. Stufkens, "Metal-To-Ligand Charge Transfer (MLCT) Photochemistry of Fac-Mn(Cl)$(CO)_3$(H-DAB): A Density Functional Study," *Journal of Physical Chemistry* 100, no. 38 (1996): 15346–15357.

52. K. Finger and C. Daniel, "Metal-To-Ligand Charge Transfer Photochemistry: Potential Energy Curves for the Photodissociation of $HMn(CO)_3$(α-diimine)," *Journal of the American Chemical Society* 117, no. 49 (1995): 12322–12327.

53. J. C. Tully and R. K. Preston, "Trajectory Surface Hopping Approach to Nonadiabatic Molecular Collisions: The Reaction of H^+ With D_2," *Journal of Chemical Physics* 55, no. 2 (1971): 562–572.

54. J. C. Tully, "Molecular Dynamics With Electronic Transitions," *Journal of Chemical Physics* 93, no. 2 (1990): 1061–1071.

55. G. Li Manni, I. Fernández, A. Galván, et al., "The OpenMolcas Web: A Community-Driven Approach to Advancing Computational Chemistry," *Journal of Chemical Theory and Computation* 19, no. 20 (2023): 6933–6991.

56. S. Villaume, A. Strich, C. Daniel, S. A. Perera, and R. J. Bartlett, "A Coupled Cluster Study of the Electronic Spectroscopy and Photochemistry of Cr(CO)6," *Physical Chemistry Chemical Physics* 9 (2007): 6115–6122.

57. F. Neese, "Software Update: The ORCA Program System, Version 5.0," *WIREs Computational Molecular Science* 12, no. 1 (2022): e1606.

58. S. Mai, P. Marquetand, and L. González, "Nonadiabatic Dynamics: The SHARC Approach," *WIREs Computational Molecular Science* 8 (2018): e1370.

59. S. Mai, D. Avagliano, M. Heindl, et al., "SHARC3.0: Surface Hopping Including Arbitrary Couplings — Program Package for Non-Adiabatic Dynamics," 2023, https://sharc-md.org/.

60. G. Granucci, M. Persico, and A. Toniolo, "Direct Semiclassical Simulation of Photochemical Processes With Semiempirical Wave Functions," *Journal of Chemical Physics* 114, no. 24 (2001): 10608–10615.

61. G. Granucci and M. Persico, "Critical Appraisal of the Fewest Switches Algorithm for Surface Hopping," *Journal of Chemical Physics* 126, no. 13 (2007): 134114.

62. G. Granucci, M. Persico, and A. Zoccante, "Including Quantum Decoherence in Surface Hopping," *Journal of Chemical Physics* 133, no. 13 (2010): 134111.

63. A. Cannizzo, A. M. Blanco-Rodríguez, A. El Nahhas, et al., "Femtosecond Fluorescence and Intersystem Crossing in Rhenium(I) Carbonyl-Bipyridine Complexes," *Journal of the American Chemical Society* 130, no. 28 (2008): 8967–8974.

64. W. Gawelda, A. Cannizzo, V.-T. Pham, F. van Mourik, C. Bressler, and M. Chergui, "Ultrafast Nonadiabatic Dynamics of $[Fe^{II}(bpy)_3]2+$ in Solution," *Journal of the American Chemical Society* 129, no. 26 (2007): 8199–8206.

Supporting Information

Additional supporting information can be found online in the Supporting Information section.